Coherent control of plasma dynamics by feedback-optimized wavefront manipulationa)

Z.-H. He, B. Hou, G. Gao, V. Lebailly, J. A. Nees, R. Clarke, K. Krushelnick, and A. G. R. Thomas

---

Articles you may be interested in

Stable laser–plasma accelerators at low densities
J. Appl. Phys. **116**, 043109 (2014); 10.1063/1.4891987

Beam loading in a laser-plasma accelerator using a near-hollow plasma channel
Phys. Plasmas **20**, 123115 (2013); 10.1063/1.4849456

Control of electron-seeding phase in a cascaded laser wakefield accelerator
Phys. Plasmas **19**, 023105 (2012); 10.1063/1.3682992

Optimization of laser parameters to obtain high-energy, high-quality electron beams through laser-plasma acceleration
Phys. Plasmas **17**, 103110 (2010); 10.1063/1.3496382

Controlling the spectrum of x-rays generated in a laser-plasma accelerator by tailoring the laser wavefront
Appl. Phys. Lett. **95**, 181106 (2009); 10.1063/1.3258022

Coherent control of plasma dynamics by feedback-optimized wavefront manipulation[a]

Z.-H. He,[1,b] B. Hou,[1] G. Gao,[1] V. Lebailly,[2] J. A. Nees,[1] R. Clarke,[3] K. Krushelnick,[1] and A. G. R. Thomas[1]

[1]*Center for Ultrafast Optical Science, University of Michigan, Ann Arbor, Michigan 48109-2099, USA*
[2]*Polytech Paris-Sud - Université Paris-Sud, 91405 Orsay, France*
[3]*Department of Physics, University of Michigan, Ann Arbor, Michigan 48109-1120, USA*

Plasmas generated by an intense laser pulse can support coherent structures such as large amplitude wakefield that can affect the outcome of an experiment. We investigate the coherent control of plasma dynamics by feedback-optimized wavefront manipulation using a deformable mirror. The experimental outcome is directly used as feedback in an evolutionary algorithm for optimization of the phase front of the driving laser pulse. In this paper, we applied this method to two different experiments: (i) acceleration of electrons in laser driven plasma waves and (ii) self-compression of optical pulses induced by ionization nonlinearity. The manipulation of the laser wavefront leads to orders of magnitude improvement to electron beam properties such as the peak charge, beam divergence, and transverse emittance. The demonstration of coherent control for plasmas opens new possibilities for future laser-based accelerators and their applications. © *2015 AIP Publishing LLC*. [http://dx.doi.org/10.1063/1.4921159]

I. INTRODUCTION

Deformable mirrors are commonly used in adaptive optical systems for correction of wavefront aberrations in high intensity laser experiments to increase the peak laser intensity, especially in systems using high numerical aperture optics. The shape of the deformable mirror is generally determined in a closed loop where either a direct measurement of the wavefront is performed[1] or an iterative algorithm is employed to optimize an experimentally measured variable as a merit signal, for example, the second-harmonic generation in a beta-barium borate crystal[2] or the third-harmonic signal at an air-dielectric surface.[3] The objective of these methods is generally to compensate for phase aberration by obtaining a flat wavefront and hence a near diffraction-limited focal profile (highest intensity/ lowest M^2 value). In principle, arbitrary intensity profile shaping may be possible, but this would require accurate knowledge of the influence function of the deformable mirror.[4] A simulated annealing algorithm was implemented to shape the focal spot towards certain pre-defined intensity distributions[5] and then extended to optimization of a laser ablation process.[6]

The measurement or determination of a process through phase control can be generalized to a set of coherent control problems, which was previously demonstrated in many different systems, including quantum dynamics,[7] trapped atomic ions,[8] chemical reactions,[9] Cooper pairs,[10] quantum dots,[11,12] and THz generation[13] to name but a few. Since the spatial phase front of the laser beam can be manipulated by a deformable mirror and a plasma wave is a coherent and deterministically evolving structure that can be generated by the interaction of laser light with plasma, it is natural to assume that coherent control techniques may also be applied to plasma

waves. Plasma waves produced by high power lasers have been studied intensively since the invention of chirped pulse amplification[14] for their numerous applications. In particular, laser wakefield accelerators[15] offer the potential for future compact accelerators thanks to the extremely large acceleration gradients generated by plasma waves that can be many orders of magnitude higher than that by conventional accelerator technology. However, although highly competitive in terms of accelerating gradient, electron beams from laser wakefield accelerator experiments are currently inferior to conventional accelerators in terms of other important characteristics, such as energy spread and stability. In addition, due to constraints in laser technology, experimental demonstrations have predominantly been performed in single shot operation, far below the kHz-MHz repetition rates of conventional accelerators.

In this paper, we demonstrate that significant improvement to electron beam properties from a laser wakefield accelerator operating at kHz repetition rate can be made through the use of a genetic algorithm coupled to a deformable mirror adaptive optical system to coherently control the plasma wave formation. When a particular wavefront of laser light interacts with plasma, it can modify the plasma wave structures and electron trapping conditions in a complex way. The manipulation of the phase/intensity structure controls the details of the propagation of the laser pulse in the plasma, which dictates the initial phase profile of the plasma wave. After the plasma wave evolves to the point of trapping, the wake phase determines the shape of the electric fields that accelerate the electron beam. For example, asymmetric wakefield can be produced with the potential for controlling electron trajectories and radiation from betatron oscillation by using asymmetric higher-order modes,[16] a wavefront with coma,[17] or a pulse front tilt.[18,19] Here, in order to implement the control, we use the scintillation

---

image of the electron beams impinging on a phosphor screen to produce a feedback for the genetic algorithm. With this method, we were previously able to increase the charge of the accelerated electrons and reduce the divergence angle significantly.[20] Here, we further show, using a "pepper-pot" emittance measurement, that direct optimization on the electron emission signal produced an electron beam with reduced transverse emittance compared to one generated by the optimized laser focus. These improvements enable potential applications using these electrons for ultrafast studies of crystalline matter.[21] In a proof-of-principle demonstration, a single-shot diffraction pattern was obtained from an oriented single crystal gold foil sample. Here we further show that optimization leads to an improved quality diffraction pattern. The feedback optimization was also used for a laser plasma experiment in which optical self-compression occurs as a result of ionization nonlinearity and spatiotemporal reshaping,[22] achieving an additional reduction in the pulse duration by applying a feedback-optimized wavefront configuration.

II. METHODS

A. Experimental setup and diagnostics

The λ^3 laser[23] system at the Center for Ultrafast Optical Science in the University of Michigan was used for these experiments, which delivers $0.8 \, \mu m$ wavelength laser pulses containing energies up to 15 mJ with a full-width-at-half-maximum (FWHM) pulse duration of close to 35 fs at a repetition rate of 0.5 kHz. After reflection from a deformable mirror with 47 mm diameter clear aperture, the laser beam was transported a distance of 4.6 m in free space onto an $f/2$ off-axis (90°) parabolic mirror inside a target vacuum chamber. Taking into account the mirror reflection loss and a probe beam split using a pellicle, approximately 80% of the total beam energy was focused within a measured focal diameter of $2.5 \, \mu m$ FWHM at the beam waist. A gas nozzle comprising a 1 cm-long fused silica capillary tubing with an inner diameter of $100 \, \mu m$ was used to flow argon gas continuously as the source for plasma target. Different plasma densities were achieved by adjusting the backing pressure and position of nozzle with respective to the interaction region, and characterized via transverse optical interferometry. The gas nozzle was typically positioned approximately $300 \, \mu m$ below the laser beam with the capillary tubing perpendicular to the beam axis. For electron acceleration experiments, the gas nozzle was placed at about $20 \, \mu m$ before the laser focus (i.e., laser pulse focused in the density down ramp); whereas for the optical compression experiments, the laser-gas interaction occurred predominantly in the out-of-focus region by placing the nozzle at $150–600 \, \mu m$ from the laser beam waist, depending on the gas species used.

The electron beam profile was measured on a scintillator plate on top of a fiber optic plate (J6677 FOS by Hamamatsu) at 35 cm downstream, imaged by a lens-coupled charge-coupled device (CCD) camera. A magnetic electron spectrometer was inserted to measure the energy distribution of the emitted electrons.

For optical pulse measurements, light transmitted through focus was collimated by a second parabolic mirror

and transported out of the vacuum chamber through a $500 \, \mu m$-thick fused silica window. An iris diaphragm was inserted to limit the beam profile for alignment in a commercial single-shot second-harmonic-generation frequency-resolved optical gating (SHG-FROG) device.[24]

B. Deformable mirror and genetic algorithm

The deformable mirror (AOA Xinetics, Northrop Grumman) has a silver coated face sheet with 37 piezoelectric actuators arranged on a square grid spaced 7 mm apart. The actuators are lead magnesium niobate ceramic capable of delivering $4 \, \mu m$ of mechanical stroke at 100 V. The mirror surface shape is controlled by setting 37 independent voltage values for the actuators by a computer genetic algorithm through the LabVIEW control environment. The voltage range applied in these experiments is 0–50 V.

The genetic algorithm is an adaptive learning method that is inspired by the process of biological evolution. It is a very useful optimization technique to solve global optimization problems in complex systems with a large number of variables. A typical genetic algorithm requires a *genetic representation* of the solution parameter space and a *fitness function* to evaluate the solutions. Here, a set of 37 values corresponding to the actuator voltage to apply for the deformable mirror constitute the genetic representation of our system. The algorithm starts with a set of solutions (population) with a pre-defined or randomly initialized genetic configuration, for example, some constant voltage on all actuators. A population of offspring containing 100 individuals is created by applying a random variation to the initial genetic configuration. Based on the goal of optimization, a fitness function is designed to produce a single-valued figure of merit (FOM) for evaluating how well an individual solves the target problem. They are to be ranked from most to least fit individuals and the best 10 individuals will be selected as new parents, simulating the survival of the fittest. A new population of 100 children is then produced using genes randomly selected from the 10 parents for each actuator.

To introduce some genetic variation to the generated children, a probability factor between 0% and 100% specified from the user interface is used for both the range of variation *and* the number of mutated genes. The genetic mutation process is important to maintain genetic diversity. These new solutions along with their 10 parents are evaluated and ranked so that the new best 10 individuals are selected as the parents for the next generation. The mixing of parents from previous generation helps retain elitism if all the children are inferior than their parents, making the algorithm more efficient. The reproduction and evaluation cycle repeats itself until a termination criteria is satisfied. The optimization results are displayed in a live graph plotting the highest FOM as a function of iteration number, which allows the user to determine if a convergence has been reached.

III. OPTIMIZATION OF ELECTRON ACCELERATION

The laser focus in vacuum was first optimized using the second harmonic signal generated from a beta barium borate crystal as the feedback signal for the genetic algorithm. The

details of this method were described in Ref. 2. The focal optimization was effective to correct for wavefront distortions in the system to achieve a close-to-diffraction-limited focus. Using the optimized focal spot, electrons were detected on the scintillator screen and the signal was maximized by scanning the nozzle position and backing pressure for appropriate plasma density condition. The sensitivity of the electron signal on the plasma densities and focal position of the gas nozzle was described in our previous paper.[25] Here, we employ fitness functions in the genetic algorithm that directly uses the outcome from the electron acceleration experiments as feedback, in particular, the CCD image of the electron scintillating signal.[20] The mirror shape that produces the best focal spot or one with a constant value voltage set to all the actuators (e.g., 30 V) is used as the initial trial solution for the genetic algorithm.

A. Electron angular profile

The schematic setup for optimizing the electron profile is shown in Fig. 1. The first fitness function we tested was based on a user-defined image mask on the image of the measured electrons. The FOM is calculated using Eq. (1), employing a multiplication of two objectives: (i) minimizing the signal outside the mask and (ii) maximizing the signal inside the mask

$$FOM = \left(1 - \frac{\text{mean intensity outside mask}}{\text{mean intensity of whole image}} \right)$$
$$\times \text{ mean intensity inside mask.} \quad (1)$$

We initialized the genetic algorithm using the mirror shape for the best focal spot and tested two different masks [see Fig. 2(a)]. Mask 1 was chosen to be on the direction of the original electron beam before optimization, while a second mask was drawn about 2 cm ($\approx 3°$) from the first one. The final results are shown in Figs. 2(b) and 2(c) after the genetic algorithm reaches convergence [Figs. 2(d) and 2(e)] within 15 min in about 30 and 100 iterations for the two

masks, respectively. The multiple lines in the convergence graphs represent the ten best individuals for each iteration. In both cases, the genetic algorithm effectively steered the electron beam to the mask area; however, the beam failed to attain the same shape and divergence for the second mask. This may be related to inherent constraints in the laser plasma conditions. For the first mask, the optimization was very effective to obtain an electron beam profile resembling the shape of the mask and increasing the total signal.

To investigate generating an electron beam with the smallest angular divergence, a second fitness function based on the image moment is defined as

$$FOM = \sum_{\substack{x, y \\ x \neq x_0, y \neq y_0}} [(x - x_0)^2 + (y - y_0)^2]^{-n/2} I(x, y), \quad (2)$$

where $I(x, y)$ is the pixel intensity for every pixel (x, y) in the whole image and (x_0, y_0) is a coordinate point in the image used as an optimization target. The power factor $n > 0$ gives higher weighting to those pixels closer to the target (inverse distance power weighting).

The pixel of the optimization point was *adaptively* adjusted (manually every 2–3 iterations) during the genetic algorithm to the peak point of the charge distribution. The first trial solution was initialized using a mirror shape with 30 V for all actuators.

Different weighting parameter n defined in Eq. (2) was tested with the results shown in Fig. 3. The best result is obtained with $n = 8$ delivering the smallest angular divergence of 7 mrad (full-width at half-maximum). The peak count and the total integrated count are increased by factors of 20 and 10, respectively, compared to the initial electron beam profile before optimization. Compared to the fitness function using the image mask approach [Eq. (1)], the number of iterations required for the genetic algorithm to converge using the image moment scheme [Eq. (2)] is typically less, taking as few as 15 iterations, which runs for 1–2 min.

B. Electron energy distribution

We extend the genetic algorithm optimization to control the electron energy distribution. A high resolution electron spectrometer using a dipole magnet pair was used to obtain the energy spectrum as the electrons were dispersed in the horizontal plane in the magnetic field. A 150 μm pinhole was placed 2.2 cm from the electron source to improve the energy resolution of the spectrometer. The schematic setup is shown in Fig. 4(a). The energy resolution due to finite pinhole size is estimated to be 2 keV for the energy range of measurement. The scintillating sensitivity for electrons in the 50–150 keV energy range was calibrated using an electron microscope.

Three rectangular masks are set in the low-, mid-, and high-energy region on the dispersed data, namely, masks I, II, and III in Fig. 4(b). The fitness function based on the image mask [Eq. (2)] was used to preferentially maximize the total counts inside the rectangular region. Fig. 4(b) shows the raw spectra after the genetic algorithm optimization and
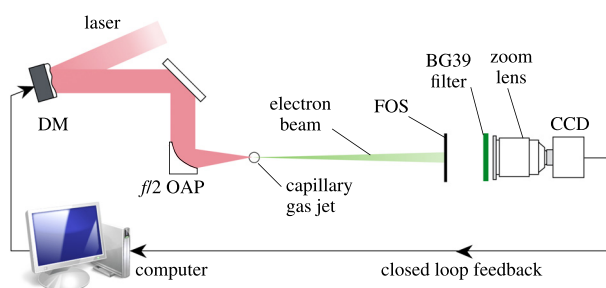

FIG. 1. Schematic of the experimental setup for direct optimization of the electron scintillating signal. The laser pulse is focused using a $f/2$ off-axis parabolic mirror (OAP) into a free flow of argon gas from a capillary gas nozzle having an inner diameter of 100 μm. A number of steering mirrors are not shown between the DM and OAP. The electrons are detected 35 cm downstream on a scintillator plate. Optical emission from scintillating screen is imaged onto the CCD to measure the electron spatial profile. The CCD images are acquired by the computer control program to be used for the genetic algorithm.
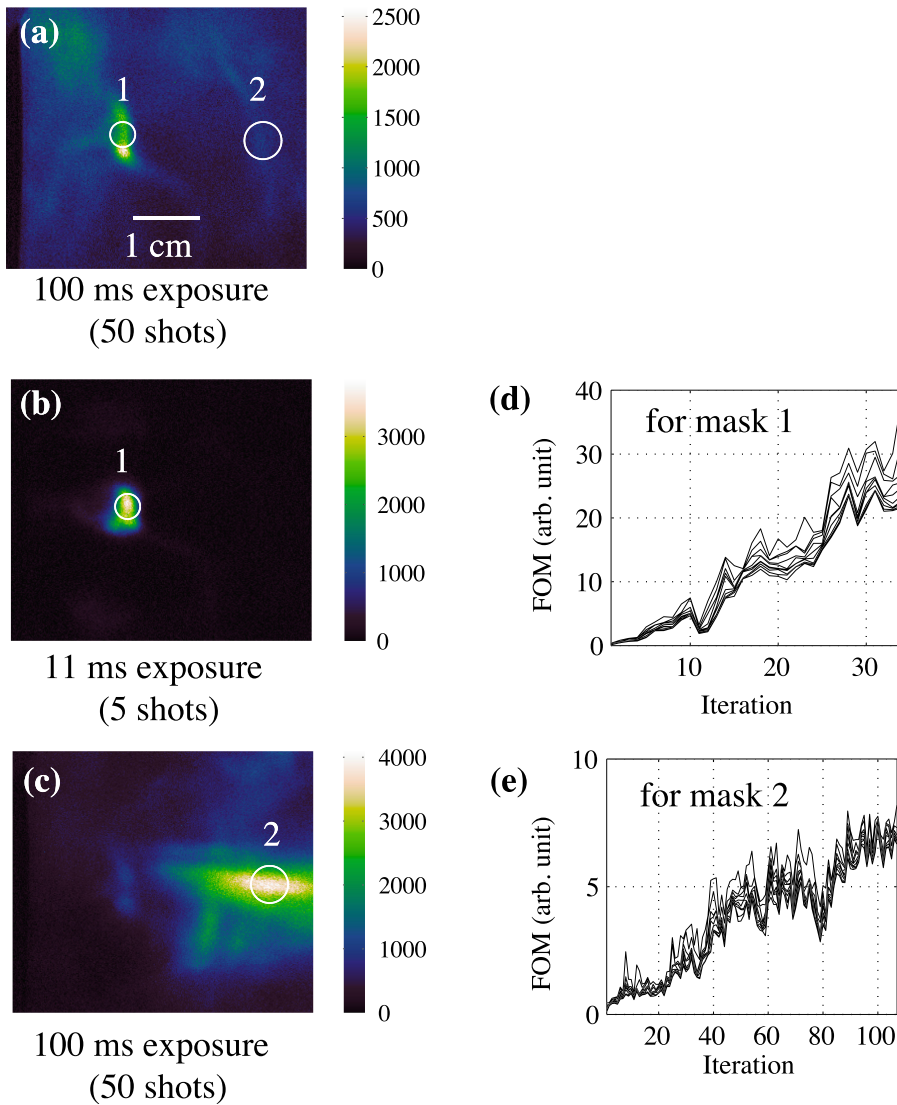
FIG. 2. (a) Electron beam profile produced with the best focal spot (optimized by second harmonic signal); (b) and (c) electron beam profiles after optimization using the circular image masks denoted by 1 and 2, respectively. Note the difference in color scale and exposure time; (d) and (e) are the genetic algorithm convergence graphs.

the brightest part has shifted congruently. The deconvolved spectra have mean energies of 89 keV, 95 keV, and 98 keV, respectively, for masks I, II, and III, noting that they do not fall on the visual centroid of the image because the scintillator sensitivity is not included in the presentation of the raw data. Our results show that manipulation of electron energy distribution using the deformable mirror is relatively restricted. Despite the fact that the mean energies can be varied by up to 10%, the final spectra after optimization does not reach the objective mask completely, in particular, for the choice of targeted region in the higher energy range (around 110 keV). This result is somewhat unsurprising as the scope for controlling the electron spectrum is mostly limited by the physics of the interaction—while changing the transverse intensity profile can make big differences to the shape of the plasma electric field structure, changing the maximum field amplitude of the wakefield (and therefore peak energy of the accelerated electrons) will be limited.

C. Transverse emittance

A more sensible property in addition to the beam profile and divergence is the emittance of the accelerated electron beam, which characterizes the momentum-position phase space distribution of the particles. It is a parameter that quantifies the beam quality and pertains to important beam characteristics such as brightness, coherence, and beam transport properties for many practical applications.

Using the pepper-pot technique,[26,27] we measured the particle distribution in the 2D subspaces of (x, x') and (y, y'), where $x' = p_x/p_z$ and $y' = p_y/p_z$ are the angles of a single electron in the beam in the horizontal and vertical directions, respectively. Following the analysis in Ref. 26, the total geometric root mean squared (rms) emittance can be obtained from the measurements, which is defined as

$$\epsilon_x \equiv \sqrt{\langle x^2 \rangle \langle x'^2 \rangle - \langle xx' \rangle^2}. \tag{3}$$

The normalized transverse emittance is given by $\epsilon_x^n = \beta\gamma\epsilon_x$, where $\beta = v/c$ and $\gamma = 1/\sqrt{1 - \beta^2}$ are the usual relativistic quantities associated with the velocity of the particle. Similar expressions can be found for ϵ_y and ϵ_y^n in the (y, y') phase space.

A 140 μm thick lead foil was used for the pepper-pot mask, with laser-machined holes having a diameter of 60 μm, in a 10 × 10 two-dimensional array spaced 500 μm
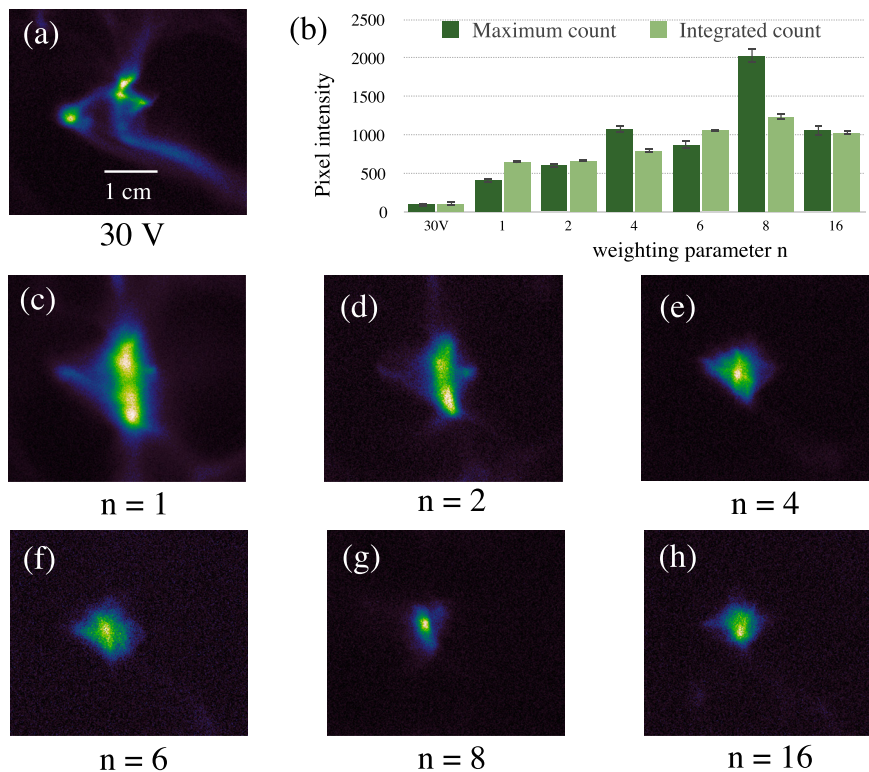
FIG. 3. (a) Electron beam profile produced by a deformable mirror shape with all actuators at 30 V accumulated over 50 shots (100 ms exposure). (b) The maximum count and integrated count (value is scaled to display on the same graph) from a *single-shot* electron image for different weighting parameter in Eq. (2). (c)–(h) Electron profile images after genetic algorithm optimization using different n.

apart. The hole mask was placed at 40 mm before the scintillator plate. The spread of divergence for electron beamlets passing through the pepper-pot mask were recorded on the screen at various transverse locations in both dimensions (x and y). Hence, the 2D hole array geometry provides information about ϵ_x and ϵ_y simultaneously. However, due to the low signal level at the phosphor screen, accumulating a sufficient number of shots is required to obtain a reasonable signal-to-noise ratio. The shot-to-shot fluctuations may be an issue, leading to overestimated values for the emittance. In fact,

compared to high energy laser wakefield experiments, the pointing and charge stability of the electron beam generated in our experiments are better.[21]

Fig. 5(a) provides a baseline of a pepper-pot image measured with a deformable mirror shape obtained from a previous optimization run on a different experimental day using the fitness functions described in Sec. III A. The beam divergence is about 10 mrad FWHM (or 3.5 mm on the detector). The rms spot widths and centroid positions of all pepper-pot beamlets are calculated and substituted into the formula in Ref. 26 for
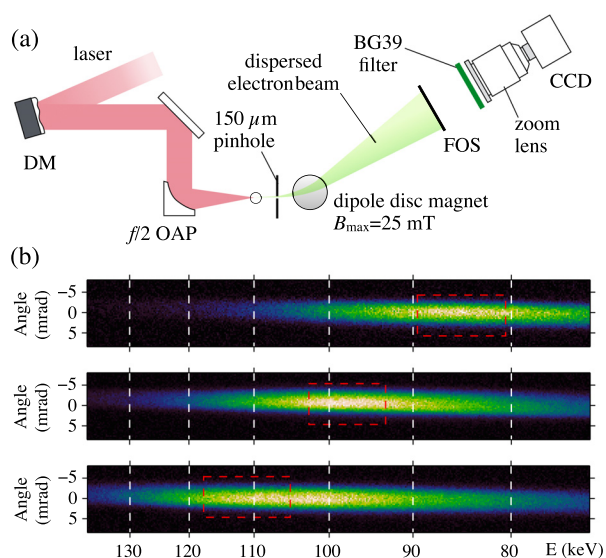

FIG. 4. Control of electron energy distribution (a) Schematic setup for measuring electron energy distribution using dipole magnets. (b) Raw data showing the dispersed electron signal after genetic algorithm optimization using three different image masks.
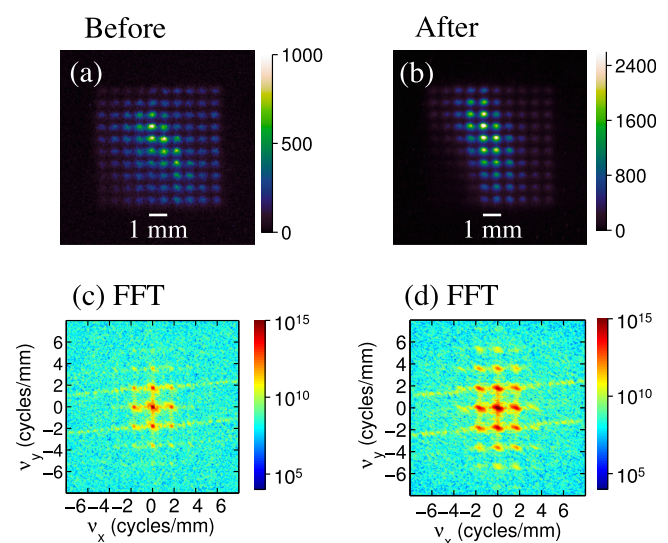

FIG. 5. Comparison of transverse emittance measurement before and after genetic algorithms. (a) and (b) Averaged pepper-pot images for a 200-shot accumulation (0.4 s exposure) generated by a deformable mirror configuration before and after genetic algorithm. (c) and (d) The corresponding FFT images displayed on a logarithmic color scale.

estimating the geometric transverse emittance. The transverse emittance for the data set in Fig. 5(a) is $\epsilon_x = 1.54 \pm 0.03\,\pi\,\text{mm} \cdot \text{mrad}$ and $\epsilon_y = 1.50 \pm 0.03\,\pi\,\text{mm} \cdot \text{mrad}$. Uncertainty values are the standard deviation from 18 consecutive 200-shot acquisition. The resolution limit of the imaging system and scintillating plate corresponds to a lower limit on the measurable emittance value about $0.5\,\pi\,\text{mm} \cdot \text{mrad}$ for our pepper-pot geometry.

Taking advantage of the periodical property of the pepper-pot mask, we applied a Fourier analysis to the measured image. A better emittance is associated with a measured pepper-pot image having smaller values in both individual beamlet sizes and the overall angular spread, which translates to having harmonics at higher order spatial frequencies and broadening of the harmonic peaks. Here, after performing a fast Fourier transform (FFT) of the experimental image data, the fitness function calculates the square of the integrated signal within the first order harmonic peak (in both x and y dimensions) as the figure of merit. After the genetic algorithm, the electron beam represented by the pepper-pot image in Fig. 5(b) has a reduced transverse emittance of $\epsilon_x = 1.20 \pm 0.08\,\pi\,\text{mm} \cdot \text{mrad}$ and $\epsilon_y = 1.34 \pm 0.05\,\pi\,\text{mm} \cdot \text{mrad}$. The total signal was also increased after the optimization. The corresponding fast Fourier transformed images for the pepper-pot measurement before and after optimization are shown in Figs. 5(c) and 5(d). During the genetic algorithm, images were acquired from the CCD camera in 2×2 binning mode to improve the signal-to-noise ratio and the computational speed, with a trade-off in spatial resolution limiting the smallest emittance measurement to $1\,\pi\,\text{mm} \cdot \text{mrad}$. Further improvement on the optimization can be expected by reducing this resolution limit and devising fitness functions incorporating more information from the analysis to offer stronger correlation to the experimental goals.

We also run the genetic algorithm for emittance starting from an electron beam already optimized by the image moment based method [see Eq. (2)]. No significant improvement was observed for the emittance, indicating that the optimization on the electron angular profile simultaneously preserves a good transverse emittance. This implies that the optimization does not significant affect the source size of the electrons (area over which they are trapped in (x,y) at the source), hence minimizing the angular spread also minimizes the emittance.

D. Electron diffraction

As we have shown previously,[21] the transverse beam quality of these electron beams is suitable for producing Debye-Scherrer ring diffraction patterns from polycrystalline aluminum samples, where visible diffraction patterns were recorded with many hundreds of shots. Here, we show that the optimized electron beam has sufficient intensity for single-shot electron diffraction from a single-crystal gold foil sample. The distance from the sample to the phosphor plate was 195 mm.

Fig. 6(a) shows the measured diffraction pattern using a single-pulse electron. Diffraction peaks from the (200) and (220) planes with lattice plane spacings of 0.204 nm and
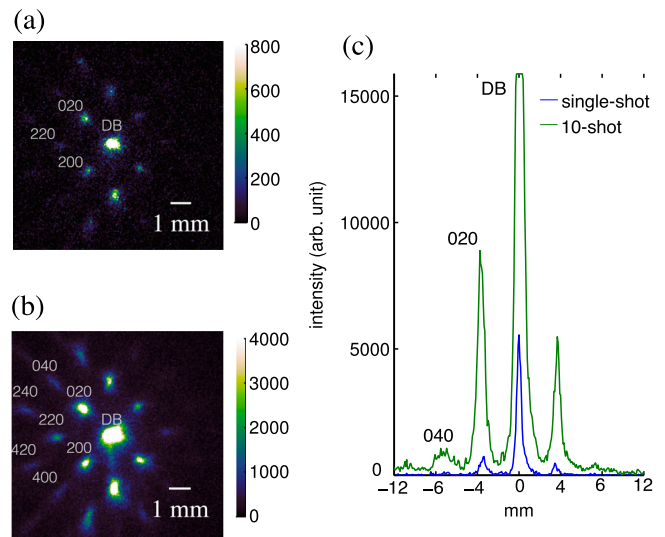

FIG. 6. Diffraction patterns obtained from a single-crystal gold foil. (a) Single-shot image and (b) 10-shot accumulation. The higher-order diffraction spots are more visible and appear streaked due to the energy spread; (c) Diagonal intensity line-out profile for (a) and (b). DB stands for direct beam.

0.143 nm, respectively, can be clearly observed from a single-shot measurement. Using the kinematic diffraction theory and the calibration lattice spacing, the location of diffraction peak centroid corresponds to electrons having energies of $105 \pm 3\,\text{keV}$, which is in agreement with the results obtained from the magnetic electron spectrometer. Second-order diffraction spots (040) can be detected with an accumulation of 10 shots [Fig. 6(b)], having a radially streaked feature as a result of the momentum spread in the electron bunch, which may be useful for time-resolved studies in streaking mode.[28]

IV. OPTIMIZATION OF OPTICAL PULSE COMPRESSION

In this section, we apply the wavefront shaping optimization to the pulse compression experiments.[22] With no changes to the experimental setup, we program the measurement result into the genetic algorithm, with a straightforward fitness function $FOM = 1/\tau_L$, where τ_L is the retrieved FWHM pulse duration from the commercial FROG device (Swamp Optics 8–9-thin-USB). The goal of the optimization is to decrease τ_L.

In Ref. 22, we have shown the pulse compression occurs as a result of complex spatial-temporal coupling induced by ionization and propagation in the mid-field region of a tightly focused laser beam. Naturally, the laser wavefront conditions are likely to play a role here. Previously, the laser focus was optimized for wavefront correction at the beam waist but it was shown that pulse compression process was not sensitive to having highest intensities at focus since the main interaction takes places at a much larger beam radius.

Fig. 7 shows the output pulse duration as a function of iteration during the genetic algorithm optimization. Argon gas was used with a backing pressure of 3.4 bar. The self-compressed pulse duration was further reduced from 30 fs to
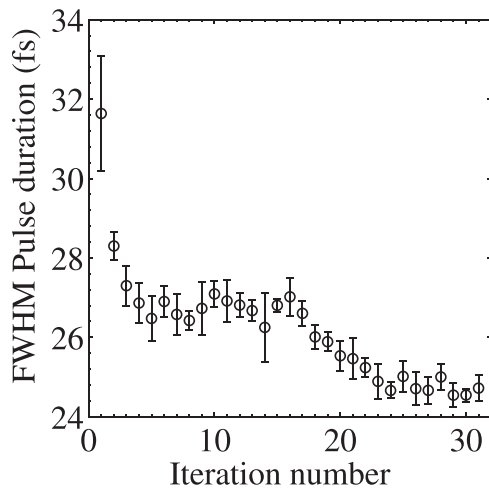
FIG. 7. Pulse compression optimization results using the deformable mirror with genetic algorithm. Error bars represent the range for the 10 best results in each iteration.

25 fs by adaptively shaping the wavefront. The original pulse duration was 36 fs for this measurement.

V. CONCLUSIONS

A feedback optimization method was implemented to improve the performance of laser wakefield acceleration through coherent manipulation of the wavefront of the driving laser pulse, enabled by the stability and high-repetition rate. The method was applied for a number of properties of the generated electron beams including their spatial profile, energy distribution, and a direct measurement on the transverse emittance, by designing different fitness functions in the genetic algorithm. The overall improvement on the beam charge and transverse coherence enables the recording of a single-crystal gold diffraction pattern using a single electron pulse, offering potential applications of a laser synchronized electron probe for structural studies of crystalline matters. The optimization process was also applied for an optical compression experiment using feedback from the FROG pulse measurement to further reduce the pulse duration.

Further improvement may be possible by increasing the number of actuators of the deformable mirror to provide finer control of the desirable phase. This will lead to increase in the computational time for the genetic search due to a larger variable space, however, a different approach for genetic representation independent of the actuator number can be employed using the Zernike polynomial coefficients.[29]

The concept of coherent control for plasmas may provide potential schemes to improve the performance of plasma-based particle accelerators. Laser wakefield accelerators are showing significant promise, but for these beams to become practical tools, many challenges remain to be overcome in terms of shot-to-shot stability and repetition rate. A recently proposed architecture[30] based on coherent combination of a large number of fibers, may offer the solution for building high power (both peak and average) and high efficiency lasers required for particle accelerator. In

principle, the coherent control methodology of this study could be applied, benefiting from the high repetition rate and phase control capability of a parallel fiber system. In addition, understanding of the stability and response of wakefield process with regard to dark current reduction and control of beam emittance is crucial for the success of laser wakefield acceleration of relativistic electrons.

[1]S.-W. Bahk, P. Rousseau, T. A. Planchon, V. Chvykov, G. Kalintchenko, A. Maksimchuk, G. A. Mourou, and V. Yanovsky, Opt. Lett. **29**, 2837 (2004).
[2]O. Albert, H. Wang, D. Liu, Z. Chang, and G. Mourou, Opt. Lett. **25**, 1125 (2000).
[3]T. A. Planchon, W. Amir, J. J. Field, C. G. Durfee, J. A. Squier, P. Rousseau, O. Albert, and G. Mourou, Opt. Lett. **31**, 2214 (2006).
[4]Z. Zeng, N. Ling, and W. Jiang, J. Mod. Opt. **46**, 341 (1999).
[5]R. El-Agmy, H. Bulte, A. H. Greenaway, and D. Reid, Opt. Express **13**, 6085 (2005).
[6]S. Campbell, S. M. F. Triphan, R. El-Agmy, A. H. Greenaway, and D. T. Reid, J. Opt. A: Pure Appl. Opt. **9**, 1100 (2007).
[7]W. S. Warren, H. Rabitz, and M. Dahleh, Science **259**, 1581 (1993).
[8]D. Wineland, C. Monroe, W. M. Itano, D. Leibfried, B. E. King, and D. M. Meekhof, J. Res. Natl. Inst. Stand. Technol. **103**, 259 (1998).
[9]A. Assion, T. Baumert, M. Bergt, T. Brixner, B. Kiefer, V. Seyfried, M. Strehle, and G. Gerber, Science **282**, 919 (1998).
[10]Y. Nakamura, Y. Pashkin, and J. Tsai, Nature **398**, 786 (1999).
[11]J. Reithmaier, G. Sek, A. Loffler, C. Hofmann, S. Kuhn, S. Reitzenstein, L. Keldysh, V. Kulakovskii, T. Reinecke, and A. Forchel, Nature **432**, 197 (2004).
[12]D. Press, T. D. Ladd, B. Zhang, and Y. Yamamoto, Nature **456**, 218 (2008).
[13]X. Xie, J. Dai, and X.-C. Zhang, Phys. Rev. Lett. **96**, 075005 (2006).
[14]D. Strickland and G. Mourou, Opt. Commun. **56**, 219 (1985).
[15]T. Tajima and J. M. Dawson, Phys. Rev. Lett. **43**, 267 (1979).
[16]Y. Glinec, J. Faure, A. Lifshitz, J. M. Vieira, R. A. Fonseca, L. O. Silva, and V. Malka, EPL **81**, 64001 (2008).
[17]S. P. D. Mangles, G. Genoud, S. Kneip, M. Burza, K. Cassou, B. Cros, N. P. Dover, C. Kamperidis, Z. Najmudin, A. Persson, J. Schreiber, F. Wojda, and C.-G. Wahlstrom, Appl. Phys. Lett. **95**, 181106 (2009).
[18]A. Popp, J. Vieira, J. Osterhoff, Z. Major, R. Hörlein, M. Fuchs, R. Weingartner, T. P. Rowlands-Rees, M. Marti, R. A. Fonseca, S. F. Martins, L. O. Silva, S. M. Hooker, F. Krausz, F. Grüner, and S. Karsch, Phys. Rev. Lett. **105**, 215001 (2010).
[19]M. Schnell, A. Sävert, I. Uschmann, M. Reuter, M. Nicolai, T. Kämpfer, B. Landgraf, O. Jäckel, O. Jansen, A. Pukhov *et al.*, Nat. Commun. **4**, 2421 (2013).
[20]Z.-H. He, B. Hou, V. Lebailly, J. A. Nees, K. Krushelnick, and A. G. R. Thomas, Nat. Commun. **6**, 7156 (2015).
[21]Z.-H. He, A. G. R. Thomas, B. Beaurepaire, J. A. Nees, B. Hou, V. Malka, K. Krushelnick, and J. Faure, Appl. Phys. Lett. **102**, 064104 (2013).
[22]Z.-H. He, J. A. Nees, B. Hou, K. Krushelnick, and A. G. R. Thomas, Phys. Rev. Lett. **113**, 263904 (2014).
[23]B. Hou, J. Easter, A. Mordovanakis, K. Krushelnick, and J. A. Nees, Opt. Express **16**, 17695 (2008).
[24]R. Trebino, K. W. DeLong, D. N. Fittinghoff, J. N. Sweetser, M. A. Krumbugel, B. A. Richman, and D. J. Kane, Rev. Sci. Instrum. **68**, 3277 (1997).
[25]Z.-H. He, B. Hou, J. A. Nees, J. H. Easter, J. Faure, K. Krushelnick, and A. G. R. Thomas, New J. Phys. **15**, 053016 (2013).

[26]M. Zhang, "Emittance formula for slits and pepper-pot measurement," Technical Report *Fermilab-TM-1988* (Fermi National Accelerator Lab., Batavia, IL, USA, 1996).

[27]Y. Yamazaki, T. Kurihara, H. Kobayashi, I. Sato, and A. Asami, Nucl. Instrum. Methods Phys. Res. Sec. A **322**, 139 (1992).

[28]E. Fill, S. Trushin, R. Bruch, and R. Tommasini, Appl. Phys. B **81**, 155 (2005).

[29]O. Albert, L. Sherman, G. Mourou, T. B. Norris, and G. Vdovin, Opt. Lett. **25**, 52 (2000).

[30]G. Mourou, B. Brocklesby, T. Tajima, and J. Limpert, Nat. Photonics **7**, 258 (2013).